

This work was written as part of one of the author's official duties as an Employee of the United States Government and is therefore a work of the United States Government. In accordance with 17 U.S.C. 105, no copyright protection is available for such works under U.S. Law.

Public Domain Mark 1.0

<https://creativecommons.org/publicdomain/mark/1.0/>

Access to this work was provided by the University of Maryland, Baltimore County (UMBC) ScholarWorks@UMBC digital repository on the Maryland Shared Open Access (MD-SOAR) platform.

Please provide feedback

Please support the ScholarWorks@UMBC repository by emailing scholarworks-group@umbc.edu and telling us what having access to this work means to you and why it's important to you. Thank you.



Influence of topology optimization parameters on the mechanical response of an additively manufactured test structure

Myung Kyun Sung^{b,1}, Matthew Schwerin^a, Yutika Badhe^{b,2}, Daniel Porter^{a,*}

^a Division of Applied Mechanics, Office of Science and Engineering Laboratories, Center for Devices and Radiological Health, United States Food and Drug Administration, Silver Spring, MD, 20993, USA

^b Oak Ridge Institute for Science and Education, Oak Ridge, TN, USA

ARTICLE INFO

Keywords:

Topology optimization
Additive manufacturing
Sensitivity analysis
Experimental validation
Worst-case
Medical

ABSTRACT

Topology Optimization (TO) determines a material distribution within a domain under given conditions and design constraints, and generally generates complex geometries as a result. Complementary to TO, Additive Manufacturing (AM) offers the ability to fabricate complex geometries which may be difficult to manufacture using traditional techniques such as milling. AM has been used in multiple industries including the medical devices area. Hence, TO may be used to create patient-matched devices where the mechanical response is catered to a particular patient. However, during a medical device regulatory 510(k) pathway, demonstrating that worst-cases are known and tested is critical to the review process. Using TO and AM to predict worst-case designs for subsequent performance testing may be challenging and does not appear to have been thoroughly explored. Investigating the effects of TO input parameters when AM is employed may be the first step in determining the feasibility of predicting these worst-cases.

In this paper, the effect of selected TO parameters on the resulting mechanical response and geometries of an AM pipe flange structure are investigated. Four different input parameters were chosen in the TO formulation: (1) penalty factor, (2) volume fraction, (3) element size, and (4) density threshold. Topology optimized designs were fabricated using PA2200 polyamide and the mechanical responses (reaction force, stress, and strain) were observed through experiments (universal testing machine and 3D Digital Image Correlation) and *in silico* environments (finite element analysis). In addition, 3D scanning and mass measurement were performed to inspect the geometric fidelity of the AM structures. A sensitivity analysis is performed to examine the effect of each TO parameters. The sensitivity analysis revealed mechanical responses can have non-monotonic and non-linear relationships between each tested parameter.

1. Introduction

Topology Optimization (TO) is a numerical optimization method that determines material distributions under objective function(s), constraint(s), and given boundary condition(s). It has solved design problems since first being introduced by Bendsoe and Kikuchi (Martin Philip Bendsoe, 1988). It has been applied to design functional structures/devices in medical (Al-Ali et al., 2017; Guo and Yin, 2019; Sutradhar et al., 2016; Wu et al., 2021), aerospace (Munk et al., 2019; Zhu et al., 2016), force transducer (Sung et al., 2022), energy harvesting

(Rupp et al., 2009; Zheng et al., 2009), electromagnetics (Deng and Korvink, 2018; Im et al., 2003; Jung et al., 2021), and fluid flow system (Gersborg-Hansen et al., 2005; Guest and Prévost, 2006) applications. Manufacturability for the topology optimized structures is a consideration that needs to be addressed due the resulting complex shape (Liu and Ma, 2016). The optimized features are often difficult to fabricate using conventional manufacturing methods (e.g., CNC machining, Electrical Discharging Machining (EDM), and laser cutting). Additive Manufacturing (AM) is one of the advanced methods that has promise in fabricating these complex geometric features (Frazier, 2014; Ngo et al.,

* Corresponding author. U.S. Food and Drug Administration Center for Devices and Radiological Health, 10903 New Hampshire Ave., WO62-2215 Silver Spring, MD, 20993, USA.

E-mail addresses: msung1@umbc.edu (M. Kyun Sung), Matthew.Schwerin@fda.hhs.gov (M. Schwerin), yutikabadhe@utdallas.edu (Y. Badhe), Daniel.Porter@fda.hhs.gov (D. Porter).

¹ Department of Mechanical Engineering, University of Maryland Baltimore County, USA.

² Department of Material Science and Engineering, The University of Texas at Dallas, USA.

2018; Wong and Hernandez, 2012). Recently, TO studies have been conducted to address design consideration and constraints for AM (Brackett et al., 2011; Liu et al., 2018; Zhu et al., 2021), such as TO design for supporting materials (Kuo et al., 2018; Vanek et al., 2014), elimination of supporting materials from filtering method (Gaynor and Guest, 2016), self-supporting structure (Langelaar, 2016), building direction (Li et al., 2020), lattice structures (Cheng et al., 2019; Xiao et al., 2018), and multi material (Gaynor et al., 2014).

Currently, patient-matched devices appear to be driven primarily by matched geometric features. These geometric features are patient-specific such as a matching bone contour interface or a matched femoral cutting guide that fits on a specific patient's anatomical landmarks. This is historically achieved through imaging techniques such as computed tomography (CT) or Magnetic Resonance Imaging (MRI), which are then segmented to create a three-dimensional (3D) model of the patient's anatomy. Afterwards the patient's anatomic 3D models are incorporated into a software workflow where the patient-matched device model is generated. Workflows in this context may be defined as providing inputs to a validated process, and then obtaining the relevant outputs. A simplified patient-match software workflow could be defined as the process of supplying patient derived 3D bone models and device design templates to a software package, generating digital designs from the software, and then verifying that the digital design is sufficient to meet the patient needs. Other workflows could be defined as also encompassing the manufacturing of the physical devices.

Patient-matched designs may not be solely limited to matching geometric features. With TO workflows and AM, it may be feasible to create patient-matched devices that accommodate a patient's physiologic mechanical needs (e.g., biologic stiffness). This could be accomplished, as an example, by using the patient's mechanical requirement as the TO objective function subject to constraints. However, determining the "design-envelope" for TO device workflows appears to have different considerations than geometrically driven patient-matched device workflows. This is due to the TO model not only being driven by the geometric inputs, but also by the objective functions (i.e., goals), constraints, boundary conditions, and loads. Medical device testing often focuses on the worst-case version(s) in a family of products and convincing an observer that the worst-case(s) have been selected for testing could require an additional amount of diligence. One effort which will be beneficial in estimating worst-case(s) is to explore the effect and sensitivity of the TO input parameters that govern the response of the workflows.

Sufficiently credible FEA models and predictable TO workflows appear to be critical when convincing technical subject matter experts that worst-cases can be identified. This work proposes to investigate the influences of TO input parameters on a simple additively manufactured pipe flange structure. The pipe flange is designed so that a vertical displacement on the offset end of the pipe creates a shear, bending, and torsional load within the structure. A center portion of the pipe is chosen to have its topology optimized. Workflows for the topology optimization and additive manufacturing process are defined. Four input parameters are chosen to vary in the TO workflow: penalty factor, volume fraction, mesh element size, and density threshold. The unoptimized and resulting topology optimized models are then additively manufactured in nylon using a laser powder bed fusion (L-PBF) system. Mechanical response Quantities of Interests (QOI) are observed and compared between simulations and experiments. Sensitives from the *in silico* model are calculated and presented.

2. Methods and materials

2.1. Pipe flange structure

A pipe flange structure is introduced for finite element analysis (FEA), topology optimization, and experimental validation. The pipe flange design is chosen due to its relatively simple nature and potential

to use analytical equations as a comparator. A Computer Aided Design (CAD) model of the pipe flange is constructed using SolidWorks (2020) Standard (Dassault Systems; Waltham, Massachusetts). Fig. 1 shows the CAD model and dimensions of the pipe flange construct which has a 5 mm thick wall. Topology optimization is performed on the middle of the structure which is indicated by red color. This region was chosen due to the limited experimental validation accessibility. The CAD model is exported as a STEP file and transferred into ANSYS Workbench 2021 R1 (ANSYS Inc.; Canonsburg, PA) to perform the static structural FEA which will then be input into the TO process. ANSYS Solid 186 element (3D solid 20 node) are used for FEA while the material properties used in the static structural FEA are shown in Table 1.

Fig. 1 shows the boundary condition of the pipe flange. Six holes in the rear of the structure (blue circles) are fully constrained. A 2 mm displacement is applied at the center of the end tab on the pipe (yellow arrow). This offset cantilever loading simultaneously applies shear, bending, and torsion to the structure. An isotropic linear elastic material model was used for PA2200 polyamide 12 and is shown in Table 1. Tensile yield properties for PA2200 can vary depending on many process variables such as laser power and velocity. Stoia et al. shows that changes to process parameters for PA2200 in a L-PBF system can alter tensile yield result from 4.35 to 22.33 MPa (Stoia et al., 2019). In this work, a conservative yield stress estimate of 15 MPa is referenced from tensile experiments in (Porter et al., 2022). This is so the reader can gauge the reported Von Mises stresses and judge if the material has potentially undergone sufficient plastic behavior, which is a behavior that is not desired for the TO and experimental methods employed.

2.2. Mesh convergence study

A mesh convergency study was performed on the static structural FEA to verify that the QOI's are sufficiently grid independent. Maximum von Mises stress is evaluated to check the mesh dependency as the element size is halved starting from 1 mm. Table 2 shows the maximum von Mises stress from different element sizes in the topology optimization region of the pipe flange. With a mesh convergence acceptance criterion of less than 5%, a mesh element size of 0.50 mm was deemed sufficient with a QOI difference of 0.12%.

2.3. Topology optimization formulation

Minimization of mechanical compliance (e.g., equivalent to maximization of the stiffness) is one of the established optimization formulations for the topology optimization (Andreassen et al., 2011; Liu and Tovar, 2014; Sigmund, 2001). The constitutive relation for this type of optimization model is shown in Eq (1) - Eq (4). Eq (1) is an objective function which is the minimization of the mechanical compliance. Constraints are volume fraction (Eq (2)), elemental density bounds (Eq (3)), and Hooke's law for FEA (Eq (4)), respectively.

$$\text{Minimize : } C(x) = \sum_{e=1}^N (x_e^p) u_e^T k_0 u_e \quad \text{Eq 1}$$

$$\text{Subject to : } V(x) \leq V_{\text{target}} \quad \text{Eq 2}$$

$$: 0 < x_{\min} \leq x \leq 1 \quad \text{Eq 3}$$

$$: KU = F \quad \text{Eq 4}$$

where C is the mechanical compliance, x is elemental density variables, P is penalty factor, u is nodal displacement matrix, k is elemental stiffness matrix, N is the number of elements used to discretize the design domain, V is volume of the optimized region, K is global stiffness matrix, U is global displacement matrix, and F is global force matrix. One of the goals of topology optimization is to obtain a binary finite solution which dictates whether elements are required (a relative density of 1 or black

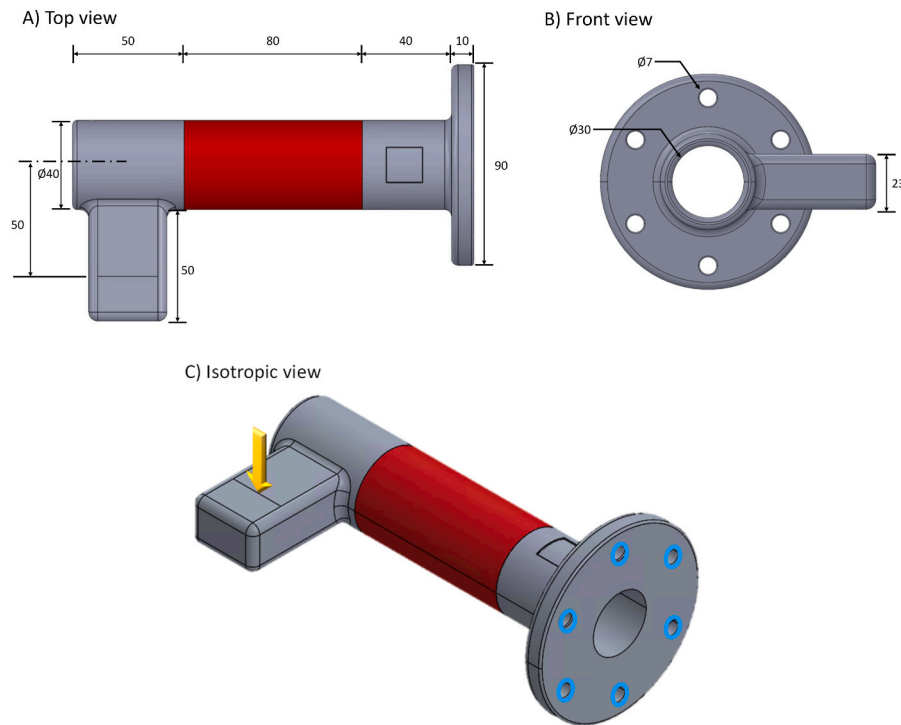


Fig. 1. Pipe flange structure A) top view, B) front view C) isotropic view with boundary and loading conditions - Yellow arrow indicates the application of the 2 mm displacement. Blue circles indicate edges which were rigidly fixed in all directions. Units are in mm. The pipe has a 5 mm thick wall.

Table 1

PA 2022 material properties used for the static structural FEA.

Property	Value	Notes
Elastic modulus (MPa)	1700	From (Porter et al., 2022) and (Neff et al., 2015)
Poisson's ratio	0.394	
Yield stress (MPa)	15	Tensile, conservative estimate from (Porter et al., 2022)
Density (kg/m ³)	930	From (PA 2200 Balance 1.0 Material Datasheet)

Table 2

Mesh convergence study for the unoptimized pipe flange static structural FEA.

Element size (mm)	0.25	0.50 ^a	1.00
Max von Mises (MPa)	2.74	2.74	2.74
Difference (%)	0.01	0.12	–
Number of elements	3,631,794	440,174	48,195

^a Chosen mesh element size for the static structural FEA which met the convergence criteria.

solution (Sigmund, 2007)) or not required (a relative density of 0 or white solution) so that an exact desired geometry can be derived. Several remedies are proposed like using a filtering method to obtain a clear solution (Guest et al., 2004; Sigmund and Petersson, 1998). Solid Isotropic Material with Penalization method (SIMP) is one of the prescribed methods that penalizes the density variables to ensure that a binary solution for the elements is obtained using a penalty factor (i.e., penalization power) (Bendsøe, 1989). Fig. 2 shows the effect of the penalty factor. When the penalty factor is 1 a linear relationship is observed but the density will be projected to smaller penalized densities as the penalty factor is increased.

If SIMP or other methods are not involved in the topology optimization, the optimization algorithm can generate a non-binary result, or grey region that is not 0 or 100% filled density. Generally, the grey region is hard to manufacture and violates mechanical responses (e.g.,

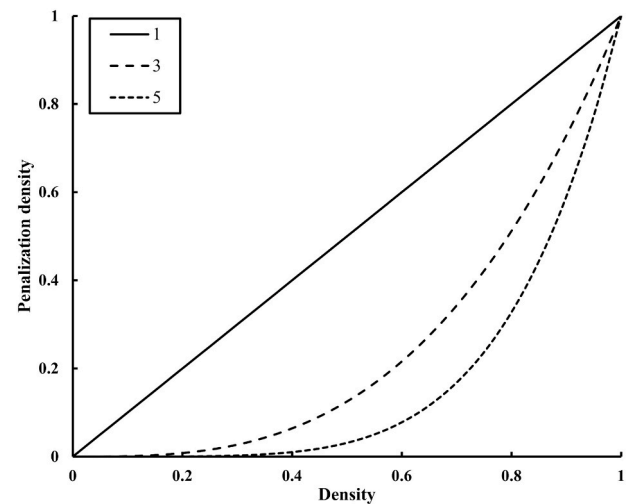


Fig. 2. Effect of different penalty factor levels on an elemental density.

stress, displacement) in the finite element analysis. Minimum density bounds (x_{\min}) are required to prevent the singularity issue when acquiring the global displacement since the stiffness matrix is influenced by elemental densities. In this work, a minimum density bound of 0.001 is used. Optimization algorithms find the optimum material distributions from objective function sensitivity information. Optimality Criteria (OC) (Zhou and Rozvany, 1991), Method of Moving Asymptotes (MMA) (Svanberg, 1987), and Level Set (Wang et al., 2003) are representative choices. In this paper, Sequential Convex Programming method (SCP) (Zillober, 1993) which is an extension of MMA is used to solve the optimization formulation. The optimization is terminated when a convergence accuracy of 0.1% or less is obtained or if the number of iterations exceeds the maximum iteration number (=500).

2.4. Topology optimization parameters and quantity of interest

Four different parameters from the topology optimization formulation are investigated to show their effects on the structure’s geometry and mechanical responses. Penalty factor (P from Eq (1)), volume fraction (V_{target} from Eq (2)), element size which is equivalent to number of elements in the topology optimization region (N from Eq (3)) are chosen in the compliance minimization formulation. Density threshold (or Retained threshold in ANSYS) which makes grey region elements into 0% or 100% density (a binary solution) from the threshold point is also investigated. For example, if the TO solution gives an elemental density of 35% and user threshold point of 50%, the elemental density becomes 0% (i.e., no material). In this work, reaction force, von Mises stress, and the first principal strain are selected for observation. The von Mises stress and 1st principal strain as well as their sensitivities to parameter changes was evaluated under an FEA parametric study. FEA reaction forces were compared to experimental applied forces in a 5 kN load frame. The first principal strains are obtained and compared from FEA and 3D digital image correlation (3D-DIC).

2.5. Workflows for topology optimization and additive manufacturing

Fig. 3 shows the defined workflow for the topology optimization process. An unoptimized design pipe flange structure is generated using a CAD program. The generated CAD file is exported to ANSYS Workbench and a static structural FEA is done with the respective loads, boundary conditions, and material models. In the static structural FEA phase, mesh parameters and topology optimization region are defined. The topology optimization requires iterative FEA to find the optimal material distributions under the given boundary condition(s), objective function(s), and constraint(s). Penalty factor and volume fraction parameters are defined before initiating the topology optimization phase and the density threshold parameter is defined after the topology optimization routine.

Table 3 shows the parameters that are investigated in this manuscript. Three values are investigated per each parameter set. Penalty factor of 3, Volume fraction of 50%, Element size of 0.5 mm, and Density threshold of 0.5 are set as reference parameters (or general optimized model – GOM). Each parameter is altered to test its effect while maintaining the other variables at the GOM setting.

Generally, topology optimized results have unsmoothed boundaries from elemental based optimization approaches. During the optimization phase, the shape and number of elements are not changed during the optimization process, only the elemental density variables are optimized. To obtain a smooth and useable CAD model, TO results require additional digital postprocessing. In this paper, SpaceClaim (ANSYS; Concord, Massachusetts) is used for digital postprocessing to remove small facets and achieve a smooth boundary from the TO design. The digital postprocessed model is transferred to ANSYS Workbench to solve a FEA model of the TO structure and obtain the *in silico* QOI’s, called a post-validation.

The workflow for the additive manufacturing process is defined as Fig. 4. First, STL files are exported from the unoptimized CAD model and the digital postprocessed topology optimized designs. The STL files are transferred to Magics 25.01 (Materialise; Leuven, Belgium) to check the geometry quality and orient the print files. The upper portion of the pipe flange loading tab was oriented parallel to the AM system’s Z axis direction (i.e., parallel to the load application from Fig. 1). While multiple

Table 3
Parameters and their values evaluated in the topology optimization workflow. The parameter levels are described as either –1, 0, or +1.

Parameter	Lower (–1)	Reference GOM (0)	Upper (+1)
Penalty factor – P	2	3	4
Volume fraction (%) - V_{target}	40	50	60
Element size (mm) – N	0.35	0.50	0.65
Density threshold	0.3	0.5	0.7

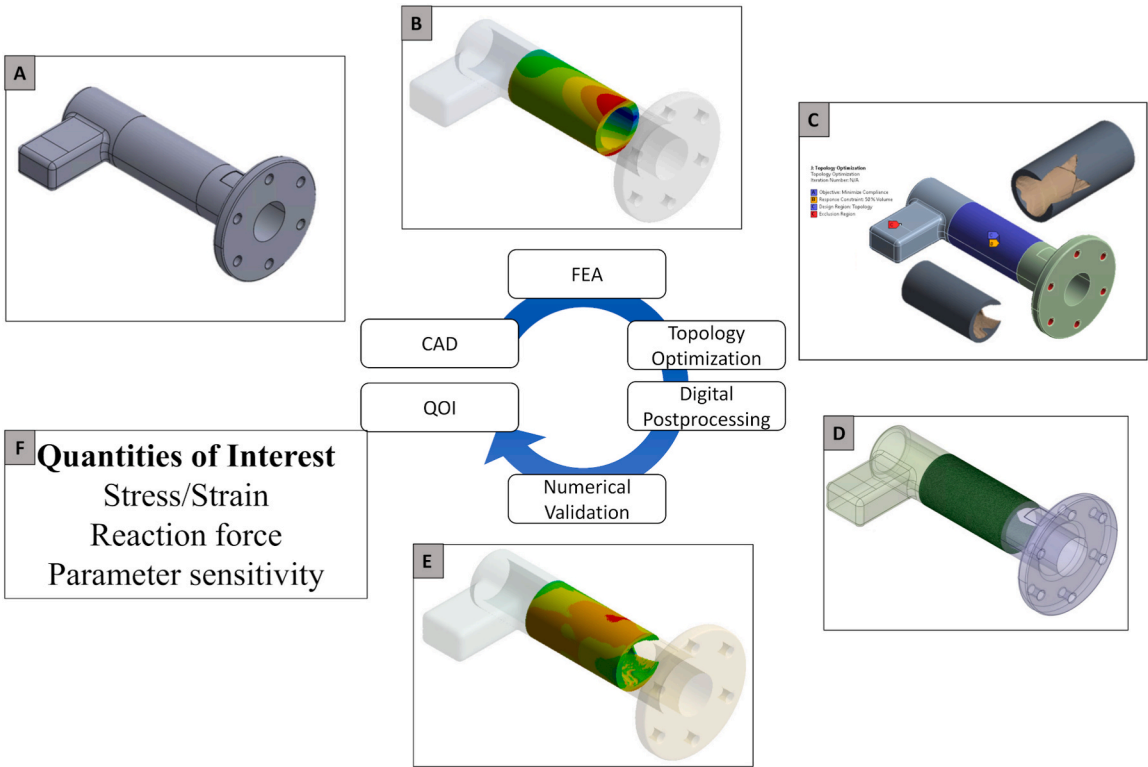


Fig. 3. Topology optimization workflow. The process includes A) an unoptimized pipe flange CAD model, B) a static structural FEA, C) topology optimization, D) digital postprocessing, E) FEA for topology optimized model, F) QOI.

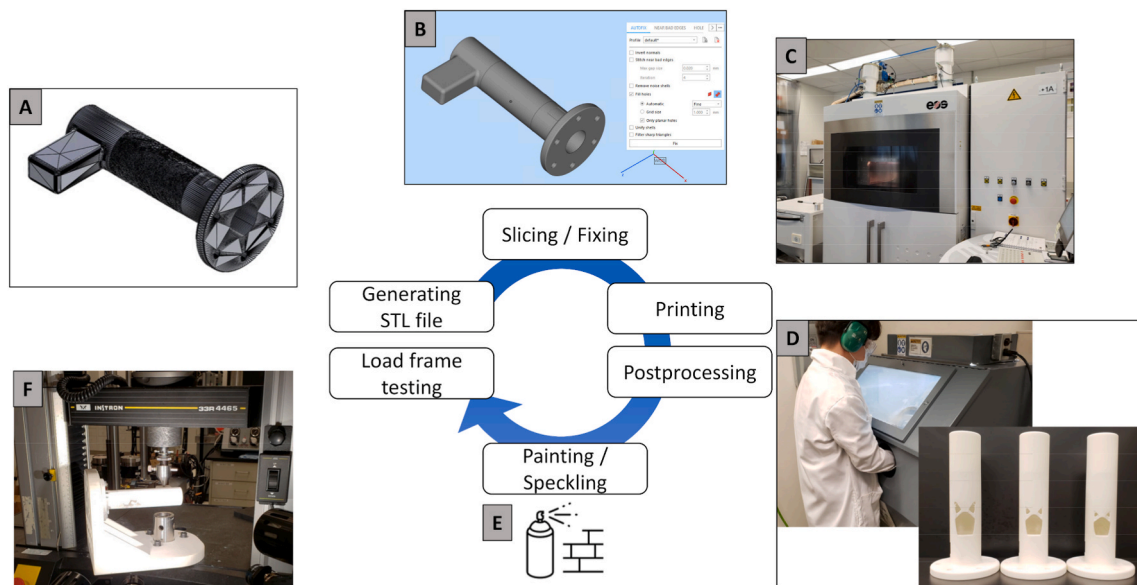


Fig. 4. AM fabrication and experimental validation workflow for the unoptimized and topology optimized structures. The process includes a) importing the STL files into Magics, B) orienting and repairing the STL files, C) printing the models in PA2200 on an EOS P396, D) post-processing the resulting structures to remove excess powder, E) speckling the structures with a matte paint, F) testing the structures in a load frame.

build orientations could have been evaluated in this work, time and budgetary limitations were prohibitive. The STLs were sliced and printed with a layer height of 120 μm in PA2200 polyamide 12 material on an EOS P396 using Process Software v3.7 Build 60 (Electro Optical Systems GmbH; Krailling, Germany). Fabricated results were extracted from the powder cake and underwent bead blasting to remove residual powder using a TRINCO Model 36/BP with 64–104 μm BT12 glass beads (TRINCO; Fraser, Michigan).

3D DIC was used to measure mechanical response of the AM specimens. Speckle patterns for tracking displacement/strain were applied to the surface of the AM specimens using paint. Fabricated samples were loaded on an Instron 33R4465 load frame with a 5 kN load cell. A fixture was designed to mount, constrain, and align the pipe flange so the load frames crosshead force was concentric (on-axis) to the pipe flange's tab feature. The fixture was fabricated using PA2200 material and used a similar AM workflow as the pipe flange samples. An assessment of the fixture's compliance at a 2 mm tip displacement is shown in [Supplement 2](#). The samples and fixture were mounted to the load frame using standard bolts, washers, and nuts. The reaction force and crosshead displacement were acquired from Bluehill software (Instron; Norwood, Massachusetts). The 3D-DIC images were acquired after stopping the load frame displacement at known intervals within the 2 mm total displacement using VIC-Snap 9 (Correlated Solutions; Irmo, South Carolina). Strain results were then processed using VIC-3D 9 (Correlated Solutions; Irmo, South Carolina).

2.6. Experimental validation

Validation studies were performed using an Instron load frame, 3D-DIC system, gravimetric scale, and 3D scanner. Five specimens for each parameter were prepared. Unoptimized and optimized areas were optically scanned using a Keyence VR-5000 3D Optical Profiler (Keyence; Osaka, Japan) to compare the design STL files to the manufactured specimens. The 3D scanner has the capability of measuring the visible surface of the specimen, but not blind features such as the interior of the structure. Due to the size constraints of the 3D scanner, separate 3D prints of only the TO region were made to facilitate measurements. Mass measurements were also acquired using a Ohaus EP6102C precision balance (Ohaus; Newark, NJ) and were compared to the STL mass derived from the digital volume and assumed constant density in

Table 1. The mass and 3D scanning comparisons provide insight into the AM System workflow's ability to accurately replicate the specimens with respect to the digitally derived designs.

After acquiring the mass and 3D metrology scans (only TO volumes), the samples were tested in a load frame and their mechanical responses were acquired. [Fig. 5A](#) shows the benchtop experiment setup for the load frame and 3D-DIC setup. The load frame crosshead speed was 5 mm/min for all experiments. 3D-DIC data were acquired and analyzed from VIC-3D software. Load frame axial force and crosshead displacement were recorded along with the 3D-DIC's 1st principal strains in the TO region of interest.

Measuring the maximum stresses and strains with 3D-DIC may not be suitable because the locations at which they occur can be located on surfaces where the 3D-DIC cameras cannot be easily observed. Therefore, 4 strain points on the outer surface of the pipe-flange are used to measure the 1st principal strains, [Fig. 5B](#). Locations of the 4 points are different for all resolved constructs due to the different optimized geometry results. These points needed to be estimated from the features present on the resulting structure and were measured by calculating distance from the concave feature of the holes using the FEA and 3D-DIC software. The strain was recorded when the pipe-flange undergoes 2 mm tip displacement from the load frame crosshead.

3. Results

3.1. Optimization and additive manufactured results

The topology optimization and additive manufacturing were performed for the stated workflows. [Fig. 6](#) shows comparisons for the optimization region between topology optimized results from the CAD program (grey) and additively manufactured results (white). The major changes are observed from the viewpoint indicated by the arrow. All designs appear symmetric at first glance, but due to the offset loading condition, they are not perfectly symmetric in design – small design changes are observed on the holes. Objective function history and a visual representation of the GOM structure as a function of solver iteration is shown in [Supplement 1 A\)](#) and [B\)](#) respectively.

The optimized geometric results for all parameters tested shows one large hole on the end of the pipe (proximal to the flange) and two triangle shape holes above the large hole (distal to the flange). Detailed

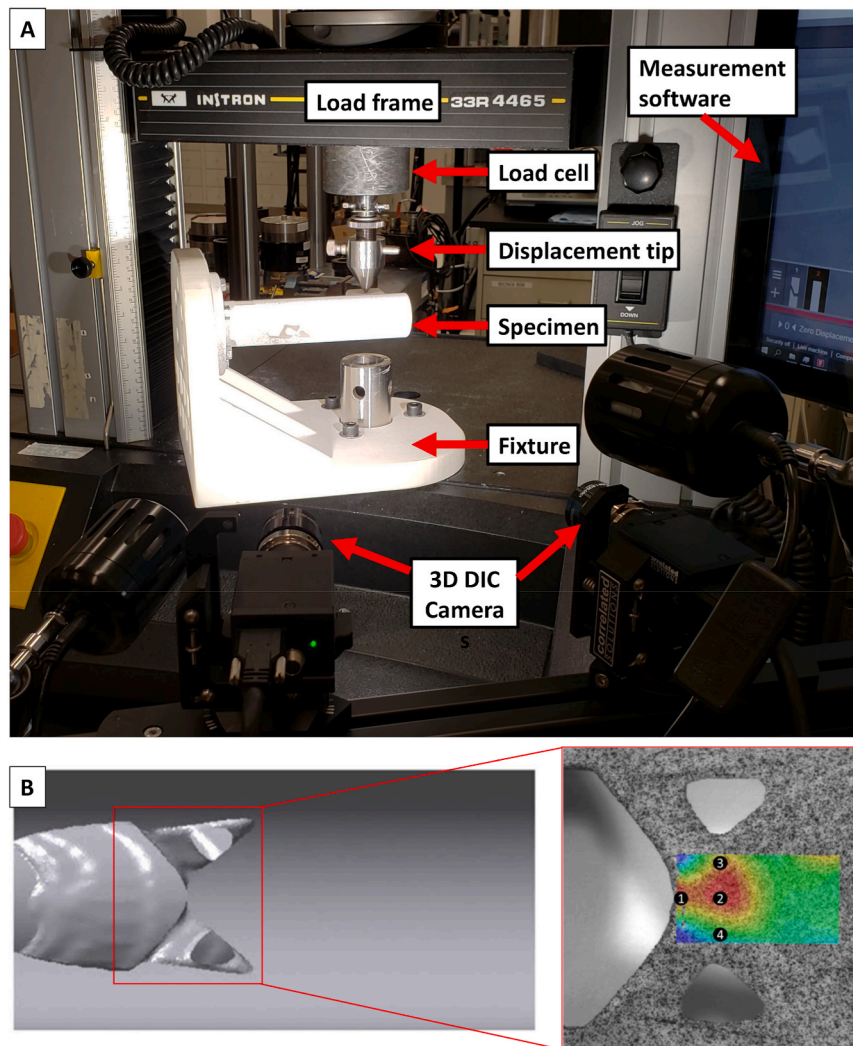


Fig. 5. A) Benchtop testing environment for the unoptimized and optimized nylon structures. B) Four points used on the FEA and 3D-DIC structure to compare 1st principal strains (shown on the GOM model).

mechanical responses are analyzed in the next section. All parameters influenced the topology optimized results. The penalty factor and mesh parameter does not affect the volume of the design, but volume fraction and density threshold point effect the topology optimized volumes.

Incrementing the penalty factor increased the size of the holes while maintaining the structure volume due to the volume fraction constraint (50%). Also, the location of the two holes is moved upward (further from the flange) as the penalty parameter is increased. The volume fraction constraint is equivalent to the retained volume of the TO solution on the optimized region of the sample. At a volume fraction of 40% the resulting design has the largest holes among the three structures and the 60% design has the smallest holes. The size of the holes also decreased as the volume fraction parameter increased. Density threshold designs are generated from the GOM by adding or removing material by adjusting the threshold parameter. The density threshold is an independent variable from the volume fraction parameter but also affects the weight of the structure. When the design has a higher threshold point, the design process removes more elements than the lower threshold point design. While a mesh grid independence study showed a converged result for the static structure FEA, topology optimized geometric results are dependent on the element size. Weight and volume are almost identical, but the results have different hole designs (Fig. 6). Again, topology optimization formulation handle “elemental” density variables that are dependent on element size and quality.

3.2. Reaction force

Reaction force linearly increased under increasing amounts of crosshead displacements. Results at a displacement of 2 mm is shown in Table 4. Overall, experimental results showed a higher reaction force than the FEA. The maximum error between experiment and FEA is 15.5% when the density threshold is 0.7. An average error of 14.0% is estimated for all parameters.

A plot of the parameter effects on the pipe flange’s reaction force are shown in Fig. 7. Penalty factor and element size are not parameters that effect reaction force since the volume of the optimized design remains the same (Fig. 7). Volume fraction and density threshold are dependent to the volume of the optimized results and causes a linear reaction force trend. As the volume fraction parameter increased, the structure requires more force to have the same displacement since the retained volume is increased. Although as the density threshold parameter increased, the structure requires less force since the retained volume is decreased. Both volume fraction and density threshold parameters show a monotonic trend with respect to the reaction force QOI.

3.3. In silico evaluation of von Mises Stress and maximum 1st principal strain

The maximum von Mises stress and 1st principal strains were

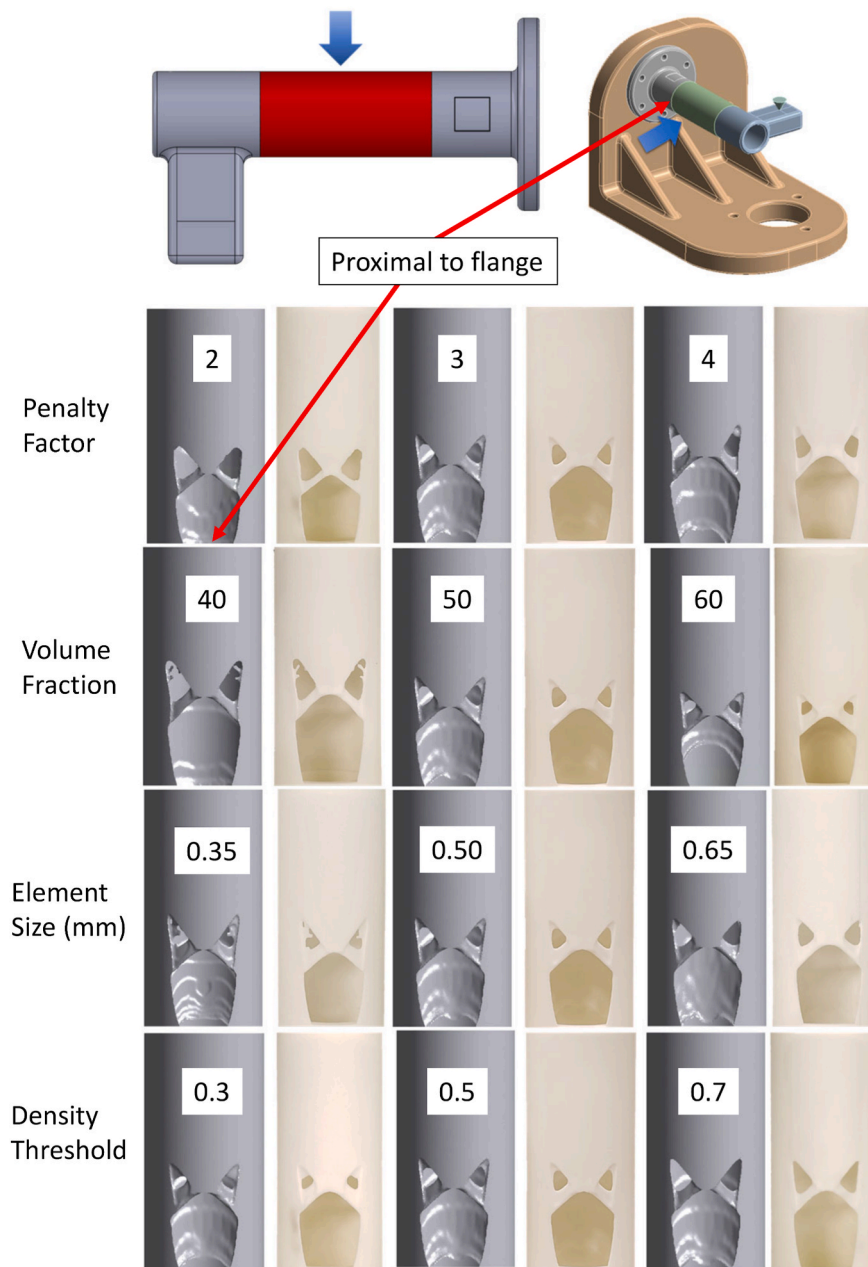


Fig. 6. Topology optimized results for all 4 parameters tested. Digital model (grey) and Additively Manufactured (white) nylon structures. Adapter jig and pipe flange structure model are shown so that image orientations are better conveyed. The GOM outputs are in the middle column.

evaluated from the FEA model. The minimum thickness of the digital structure was not controlled during the TO process in these efforts. This would generally be controlled to at least the minimum feature capability of the AM technology used to fabricate the structure. Geometric optimization results can derive very thin features (less than 0.2 mm) that is not easily manufacturable with a given AM system and can give rise to large errors in FEA QOIs when compared to experimental results.

Thin features which may not be accurately resolved on the AM system are identified near the two holes present on the optimized models (Fig. 8A). These thin features are near the resolution limits of the given EOS AM system and may cause high errors in the stress and strain mechanical response validations. To easily record maximum FEA von Mises stress and strains which do not consider these potentially erroneous geometric features, they are omitted from the model after the FEA solutions are obtained. These thin features are shown in the von Mises stress contours in Fig. 8B while they are omitted in the postprocessing in

Fig. 8C.

Table 5 shows the FEA maximum von Mises Stress, maximum 1st principal strain, and their respective sensitivities for the topology optimized section after excluding thin features. Removal of the thin features from the solution domain does affect the resulting QOI. The maximum stress is found to be 8.99 MPa in the original FEA GOM model but was 3.26 MPa after excluding thin features. Sensitivities are calculated with respect to the GOM and are intended to show how much the *in silico* QOI would change with a local adjustment of the parameters being studied. When the thin features are excluded, the largest difference in max von Mises stress as a function of the parameter levels was 172, 44, 165, and 36% for the penalty factor, volume fraction, density threshold, and element size, respectively. The largest difference for the max 1st principal strain was 140, 53, 143, and 29% for the penalty factor, volume fraction, density threshold, and element size, respectively. Volume fraction appeared to have a constant sensitivity to max von Mises and

Table 4

Reaction force results for the unoptimized GOM and parameter studies. Experimental means are presented with \pm standard deviations ($n = 5$). The parameter levels are described as either -1 , 0 , or $+1$.

	Experimental (N)		FEA (N)		Error (%)	
Unoptimized GOM (0)	112.5 \pm 2.8		106.4		7.9	
	109.1 \pm 1.6		95.3		14.4	
	Lower (-1)	Upper ($+1$)	Lower (-1)	Upper ($+1$)	Lower (-1)	Upper ($+1$)
Penalty factor	108.9 \pm 2.3	108.1 \pm 1.1	95.5	95.1	14.1	13.7
Volume fraction (%)	98.7 \pm 1.0	114.9 \pm 1.2	88.6	100.3	11.5	14.6
Density threshold	110.9 \pm 3.5	107.7 \pm 1.4	97.0	93.2	14.3	15.5
Element size (mm)	109.4 \pm 2.6	108.3 \pm 2.3	95.4	95.2	14.7	13.8

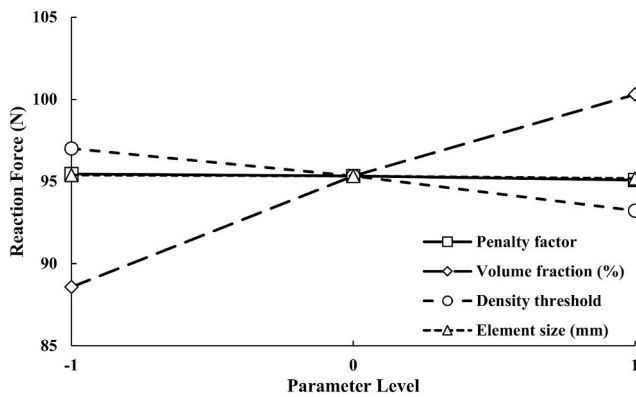


Fig. 7. FEA reaction forces for all parameters tested. Volume fraction and density threshold drive the structures' reaction force linearly.

maximum 1st principal strain in the ranges tested.

Plots of the QOI's as a function of parameter levels are shown in Fig. 9. The observed stress and strain trends were non-linear and non-monotonic. This contrasts with the reaction force QOI which showed linear trends when the volume fraction and density threshold parameter changed. The stresses and strains are not identical due to the different topology optimized geometry results. GOM has a lower maximum von Mises stress than the optimized designs. Stress concentrations not located on thin features are found for penalty factor 2 and density threshold 0.7 models. These models show higher stresses than other designs.

3.4. 3D scanning and mass measurement

Optically scanned images, estimated heights, and the height difference between STL and measurement scan of the unoptimized model is shown in Fig. 10A, B, and C respectively. Some symbols are marked on the structure to identify the subspace on the scanning surface and help "stitch" the images together in the scanner's software. The unoptimized model with a 5 mm thick wall shows less than a 0.1 mm height difference between the STL and scanned model. However, thin features from the topology optimized model are identified from the scanned model and are further inspected. A height difference map for the GOM is shown in Fig. 10D and has a user selected sub section of a thin region which is indicated by a red arrow. The user selected sub section heights from the STL, the scanned data, and a height difference between STL and scanned data are presented in Fig. 10E. From the user selected sub section, a maximum height difference of 0.306 mm is observed which is larger than the minimum XY feature resolution of the AM workflow (about 0.2

mm). The resulting height profiles of the STL and scanned component generally have the same trend and it appears the AM process adds more material for thin features than the assigned STL file prescribes.

Mass measurements and digital volumes for the unoptimized and optimized regions of all designs are shown in Table 6 ($n = 1$). Two factors are compared; the mass between the STL and manufactured construct to check for fabrication fidelity, and the ratio between unoptimized and optimized models to check for the retained volume fraction fidelity. The results help verify that the given AM process generally adds more material than the STL file specifies as discovered in the 3D scanning efforts. The maximum error between manufactured results and STL file is found to be 5.7% for the GOM. Volume fraction parameters generally agreed well with the generated STL volumes but around 3% mass difference was observed between all manufactured results and the STLs for the mass ratios relative to the unoptimized design.

3.5. 1st principal strain validation

Visual comparisons between the 3D-DIC and FEA 1st principal strains on the GOM are shown in Fig. 11. While the strain magnitudes may be different, a similar trend is observed between them. Table 7 summarizes the 1st principal strains from FEA and 3D-DIC. DIC strains are averaged from 5 specimens and are shown with 1 standard deviation to gauge repeatability.

The largest mean 1st principal strain error for Location 1, 2, 3, and 4 was 27.6, 13.4, 21.3, and 30.0% respectively. The average error for all mean comparisons is 11.6% with the maximum error being the Penalty Factor 2 case, at location 4. Location 2 showed the smallest maximum error when compared to Locations 1, 3, and 4 which may be due to the edge effects of 3D-DIC analysis. The data at the edges of the contour area tends to be influenced more by the 3D-DIC algorithms and filtering effects since there are fewer points to track. Even so, the 3D-DIC approach can be a complementary validation method that captures stress and strain trends of the additive manufactured structure. No single challenged parameter appeared to govern the magnitude of 1st principal stress validation errors.

4. Discussion

Understanding the effects of the TO workflow parameters on predicting QOI's is important. Two of the TO workflow parameters evaluated around the GOM in this effort, volume fraction and density threshold, appeared to have a linear relationship with respect to the entire construct's systematic reaction force (Fig. 7). The other two parameters, penalty factor and element size, did not appear to have a significant impact on the entire construct's systematic reaction force when evaluated around the GOM. Had the performance of the construct been judged solely on the construct's reaction force, then it may be reasonable to attempt estimations of the worst-case parameters which derive the weakest reaction force design. However, some parameters considered for local mechanical responses (e.g., local stresses and strains) revealed highly non-linear and non-monotonic trends. Additionally, the sensitivity of these parameters changed depending on which way the parameter was altered from the GOM. This is important because non-linear and non-monotonic trends of performance predictors may make estimating and extrapolating worst-case design(s) complicated. Local mechanical responses are also used as predictors of static and fatigue failure (e.g., von Mises yield criterion, fatigue fracture). Montoya-Zapata et al. found similar behaviors from varying the penalty factor and filter radius for a topology optimized simple beam which revealed differing structures. For their beam problem increasing penalty factor appeared to cause a convergence of max von Mises stress while increasing the filter radius showed non-monotonic max von Mises trends (Montoya-Zapata et al., 2019). Future research in exploring how TO parameters can be sufficiently bounded into a well-known "design envelope" to control and predict worst-cases designs should be explored.

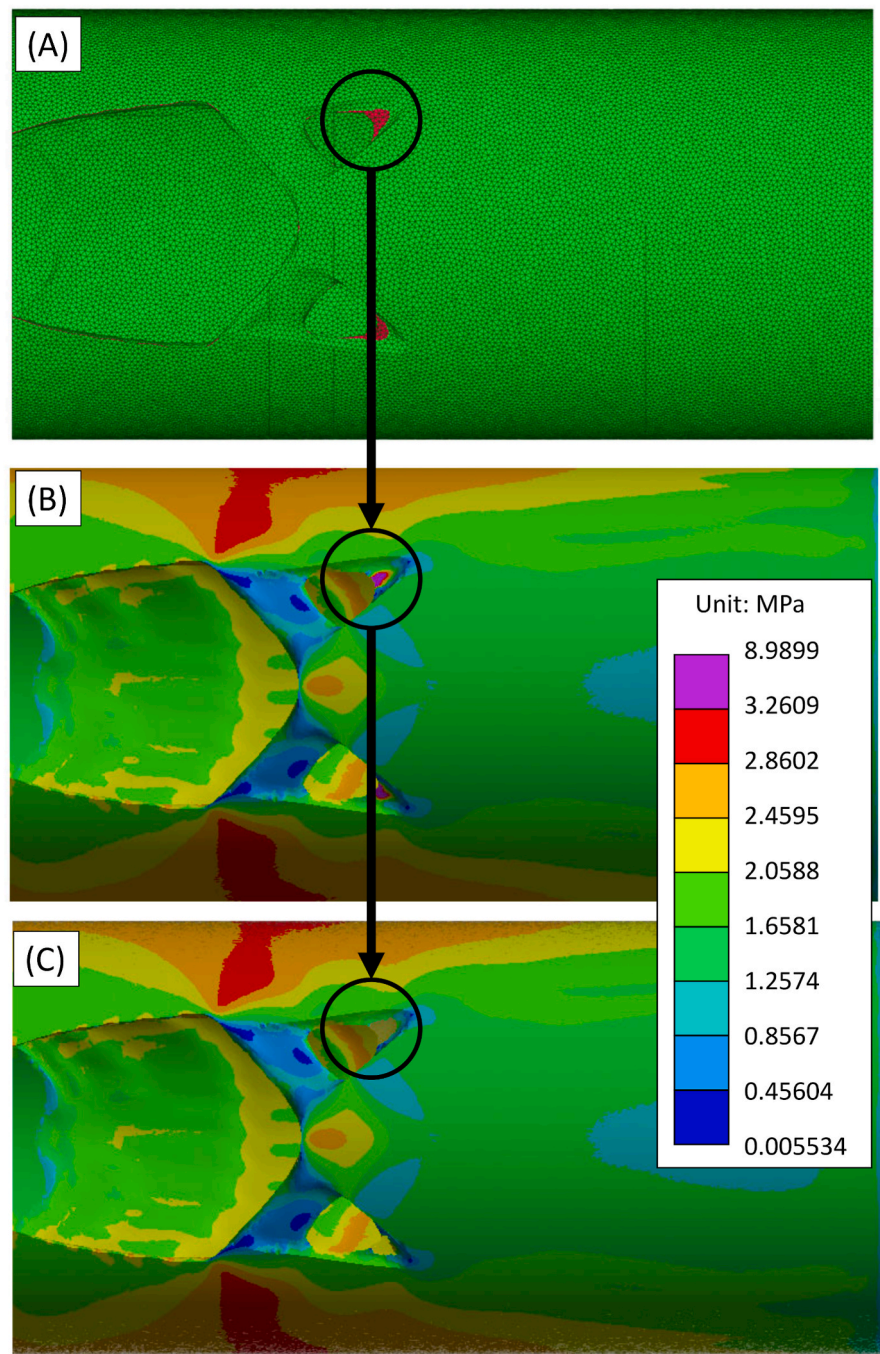


Fig. 8. A) Thin features (less than 0.2 mm) on GOM which may not be accurately fabricated on the AM system. B) High stress areas for the thin features. C) Thin features removed from the solution domain.

Table 5

Von Mises stress and 1st principal strain results for the FEA post validation simulation with the thin features excluded. Sensitivity values are calculated relative to the GOM. Δ Parameter is the change in parameter value from the GOM parameter value. The parameter levels are described as either -1 , 0 , or $+1$.

	FEA Max von Mises (MPa)				FEA Max 1st Princ. Strain ($\mu\epsilon$)			
	Lower (-1)	Upper ($+1$)	Sensitivity (Δ MPa/ Δ Param)		Lower (-1)	Upper ($+1$)	Sensitivity ($\Delta\mu\epsilon/\Delta$ Param)	
Unoptimized	2.75				1586			
GOM (0) [3, 50, 0.5, 0.50]	3.26				1817			
			Lower (-1)	Upper ($+1$)			Lower (-1)	Upper ($+1$)
Penalty factor [2,4]	8.88	4.19	-5.61	0.93	4361	2179	-2544	362
Volume fraction (%) [40, 60]	4.60	4.71	-0.13	0.14	2728	2779	-91	96
Density threshold [0.3, 0.7]	3.33	8.65	-0.36	26.93	1818	4421	-2	13018
Element size (mm) [.35, .65]	4.42	3.89	-7.74	4.18	2268	2346	-3005	3527

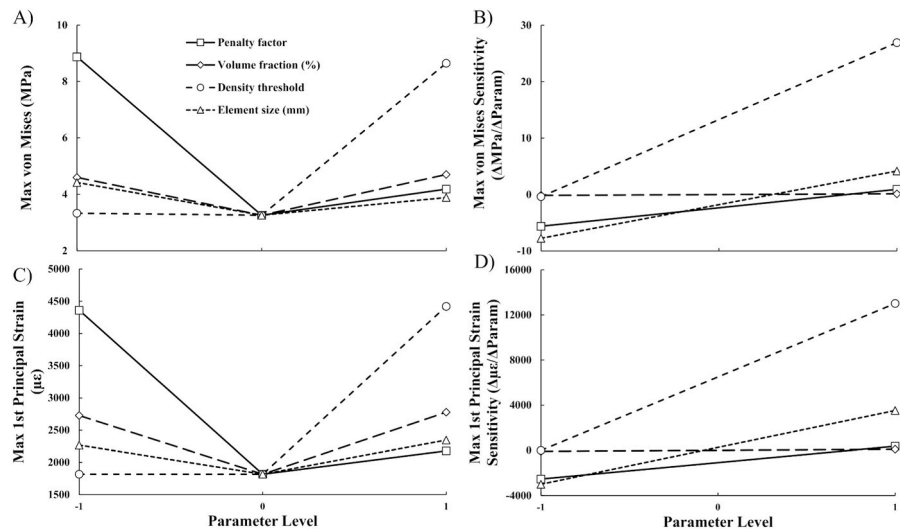


Fig. 9. FEA A) maximum von Mises Stress values and B) sensitivities for the tested parameters. FEA C) maximum 1st principal strain values and D) sensitivities for the tested parameters. Thin features are excluded. Sensitivity values are calculated relative to the GOM. Δ Parameter is the change in parameter value from the GOM parameter value. The parameter levels are described as either -1, 0, or +1.

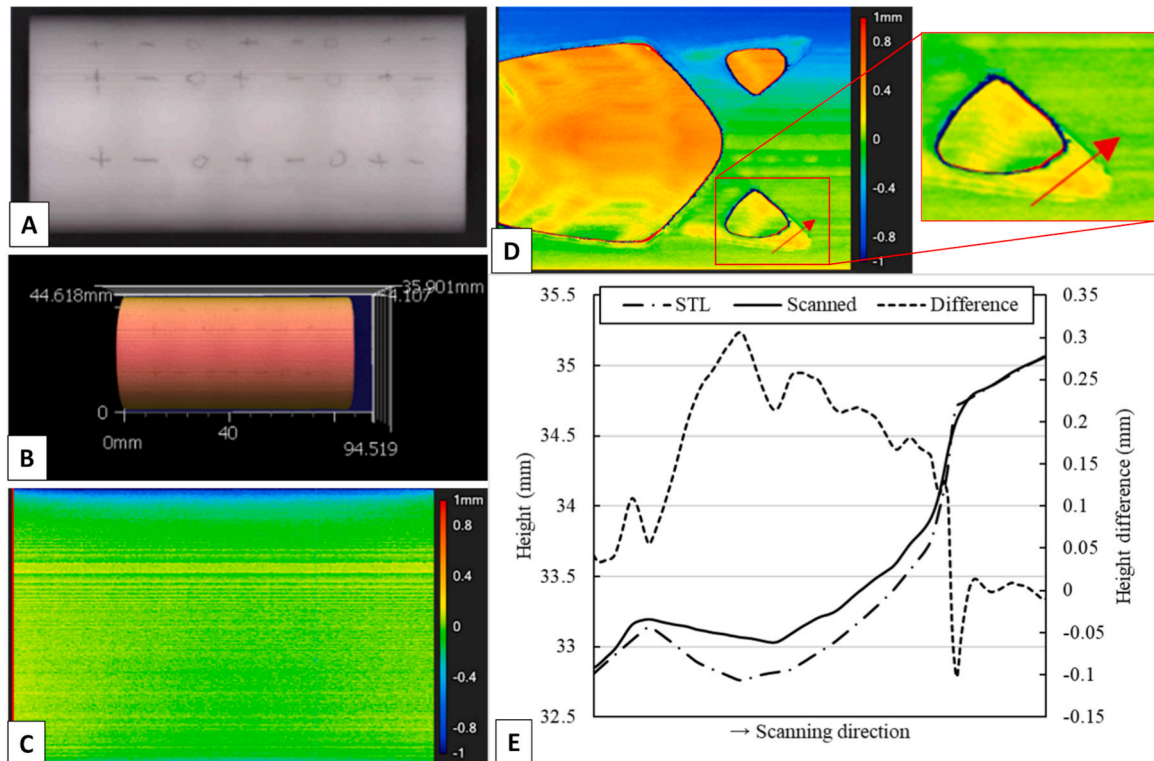


Fig. 10. A) Optical scan image of unoptimized nylon sample in the TO region of interest with B) height measurements. C) Height difference error map comparison of the unoptimized 3D scan and STL file (units in mm). D) Height difference error map comparison of the GOM model in the TO region of interest with a sub-section analysis indicated by a red arrow. E) Sub section analysis along the red arrow showing comparison between the STL, scanned surface, and the error between the two.

All TO workflow parameters evaluated in this effort appeared to alter the final geometric features of the tested pipe-flange. Some of the derived features were also smaller than the AM system's resolution capability ($\sim 200 \mu\text{m}$ in the XY) and required careful consideration when interpreting FEA and 3D-DIC local mechanical responses. An example of this is the 1st principal strain comparisons in the TO region of the construct. Errors as high as 30.0% were observed between the 3D-DIC and FEA post-validation (static structural analysis after TO material removal and filtering). There are many avenues of explanation of why

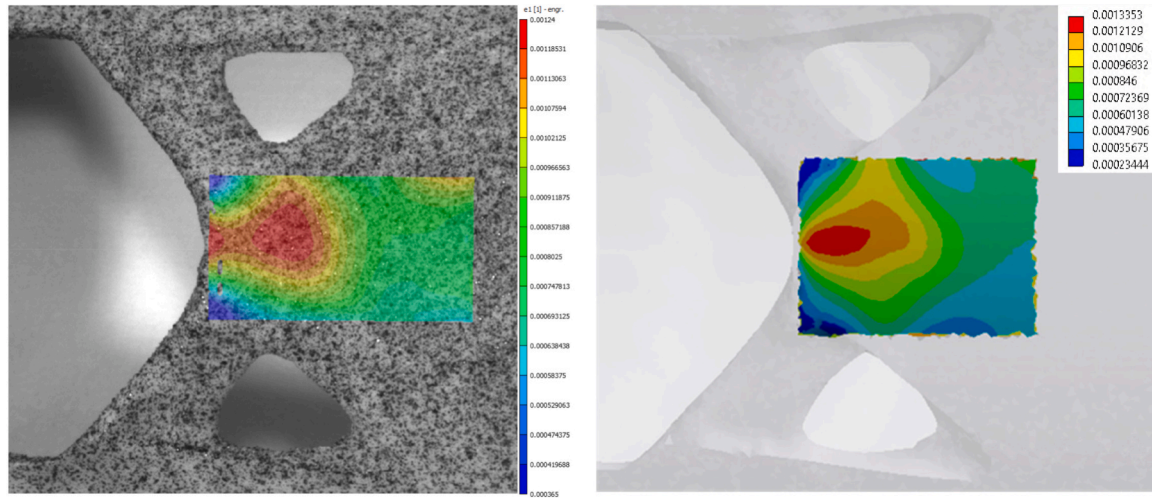
this may be and even interesting observations regarding the capacity of predicting and maintaining a worst-case construct.

For one, validating local mechanical responses around small sharp and potentially blind corners can prove difficult. This is important since TO tends to derive these organic corner features during the optimization process and these same corners features may be the source for high stress risers (a potential failure predicting location). Stress risers may be difficult to account for when using topology optimization and assessing the credibility of certain computational models. Tyflopoulos et al.

Table 6

Mass measurement comparisons between the manufactured construct and nominal STL design for all designs (n = 1).

		Manufactured (g)	STL (g)	Error (%)	Mass ratio from Unoptimized (%)		Volume from STL (mm ³)
					Manuf.	STL	
Unoptimized		41.39	41.78	−0.94			43,981
GOM		22.10	20.90	5.73	53.4	50.0	22,002
Penalty factor	2	21.81	20.87	4.53	52.7	49.9	21,963
	4	21.57	20.91	3.18	52.1	50.0	22,005
Volume fraction	40%	17.41	16.70	4.23	42.1	40.0	17,582
	60%	26.21	25.10	4.43	63.3	60.1	26,420
Density threshold	0.3	22.99	22.45	2.39	55.5	53.7	23,634
	0.7	20.01	19.34	3.48	48.4	46.3	20,355
Element size	0.35 mm	21.62	20.89	3.50	52.2	50.0	21,987
	0.65 mm	21.77	20.90	4.16	52.6	50.0	22,001

**Fig. 11.** 1st principal strain contour comparison between DIC (left) and FEA (right). Left contour ranges from 1240 $\mu\epsilon$ (red) to 365 $\mu\epsilon$ (blue).**Table 7**Mean 1st principal strain ($\mu\epsilon$) comparisons between FEA and 3D-DIC on 4 selected points for all optimized structures. Mean \pm 1 standard deviation (n = 5).

Parameter Level			1	2	3	4
GOM	3, 0.5, 50, 0.50	FEA	1260	1200	1000	760
		DIC	1090 \pm 133	1290 \pm 104	1150 \pm 245	780 \pm 158
		Error (%)	14.0	7.4	15.0	2.8
Penalty Factor	2	FEA	1820	1520	1470	1080
		DIC	1590 \pm 214	1610 \pm 117	1360 \pm 176	1430 \pm 118
		Error (%)	12.8	5.5	8.1	32.1
	4	FEA	1210	1190	920	900
		DIC	1270 \pm 95	1340 \pm 30	850 \pm 84	970 \pm 44
		Error (%)	5.2	12.6	7.3	8.3
Density Threshold	0.3	FEA	1070	940	790	720
		DIC	890 \pm 80	1010 \pm 99	830 \pm 107	860 \pm 97
		Error (%)	17.1	6.7	5.0	19.3
	0.7	FEA	1590	1590	1480	1070
		DIC	1180 \pm 72	1370 \pm 113	1160 \pm 79	1090 \pm 136
		Error (%)	25.8	13.4	21.3	1.3
Volume	40	FEA	1500	1740	1670	1130
		DIC	1350 \pm 96	1790 \pm 153	1780 \pm 152	1210 \pm 61
		Error (%)	9.9	3.0	6.2	7.4
	60	FEA	1060	980	810	710
		DIC	940 \pm 232	1120 \pm 107	820 \pm 128	920 \pm 110
		Error (%)	11.8	13.9	1.4	30.0
Element Size	0.35	FEA	1240	1270	1120	760
		DIC	900 \pm 116	1130 \pm 81	950 \pm 83	760 \pm 158
		Error (%)	27.6	10.9	15.3	0.5
	0.65	FEA	1230	1330	1140	870
		DIC	1110 \pm 119	1460 \pm 257	1140 \pm 147	1020 \pm 155
		Error (%)	9.6	10.1	0.4	18.2

evaluated ten different design processes of which three involved only topology optimization and three involved a combination of parametric and topology optimization. Maximum stress in their optimized components varied from ~28 to 118 MPa in one design process for a hollow plate, L-bracket, and Messerschmitt–Bölkow–Blohm Beam. Tyflopoulos et al. states that while their results obeyed stress conditions imposed on the models, stress-based optimization is far more complicated than compliance minimization (Tyflopoulos and Steinert, 2020).

Additionally, if the models are to be credible, then the FEA models will need to use accurate material models to predict the optimized constructs performance. Material models are generally derived using tensile or compression specimens whose gauge section is on the order of a few to tens of mm. If the AM process needs to replicate feature sizes which would invalidate the material model's fidelity due to differences in processing conditions (e.g., small features may have drastically different time-temperature profiles during the AM build process), then additional source of error could be introduced.

An AM system's ability to accurately replicate the optimized constructs derived geometric features will be critical if the features are in locations that govern static or fatigue failure. If a thin portion of the digitally derived construct is specified to be 300 μm thick, but the AM process physically replicates the feature at 250 or 350 μm , this could significantly change the FEA's predicted performance. As mentioned in this manuscript, some of the resolved features in the TO designs where near or under the AM systems 200 μm XY resolution limit. This appears to have occurred even though a mesh element size of 0.50 mm was deemed sufficient for grid independence with respect to max von Mises (Table 2).

The above explanations may offer some insight into why the authors obtained a high error during the local mechanical response validations. Other influences such as potential residual thermal stress from the AM process could also impact the performance of the fabricated construct. To mitigate these potential pitfalls, it may be beneficial for TO workflows to account for the AM systems resolution limits and potential mechanical property changes (e.g., feature size driven changes in mechanical properties) by first understanding the limits, and then imposing controls in the TO process to ensure these issues have a high probability of not arising during the workflow. Another potential avenue of amelioration is to impose controls in the TO workflow that ensure the locations of the performance predicting QOI's always occur in easy to validate locations, such as thicker and visible static landmarks (i.e., are not modified by TO). Well applied stress constraints may also help drive the governing QOI's to these landmarks.

Ensuring that QOI's are sufficiently mesh grid independent is essential in establishing credible, performance predicting, *in silico* models. The resulting geometries and features that are derived using the TO workflow herein appear to be dependent on the initial static FEA element sizing. This element size dependence is intuitive because the elements, whose size and shape are generally set prior to the TO elemental density calculations, are assigned a graded criteria which determines if the element is deleted or retained. Similar observations of 2D mesh size dependence can be found in Keshavarzzadeh et al. work (Keshavarzzadeh et al., 2019). The optimal geometries of the construct, again based on the different initial element sizing, appears to cause certain features to also evolve differently as seen in Fig. 6. Considering that most elements used in 3D FEA models tend to have sharp corners, a process that selectively removes those elements to accommodate a prescribed optimal solution would most likely leave sharp and undesirable features. Geometric filtering is required to obtain smooth, final designs. When predicting worst-case optimized designs, the elemental size dependence as well as the filtering process should be considered. Sotola et al. found that solutions of a topology optimized cantilever beam differed when using different elements and filter parameters (Sotola et al., 2021). They also found that penalty factor was a key parameter in their model. It may be beneficial for future research to focus on controlling or limiting this mesh size dependence either

through workflow methods or programmatically in the TO software (e.g., minimum manufacturability thickness of the structure or to enforce stress constraints).

Additional limitations of this work may be that designs and modeling conditions other than the pipe-flange construct may reveal different observations. The pipe-flange was chosen due to its simplistic nature to fabricate and assumed validation simplicity. Component build angle dependence may need to be explored if the construct is intended to have various build orientations (only a single build orientation was evaluated in this works). Also, different material models or geometric nonlinearities in the digital FEA workflow could also alter the results.

5. Conclusions and future work

This work explored topology optimization parameter effects on the mechanical responses of an additively manufactured pipe flange structure. This was done with a focus on assessing if estimating a worst-case (e.g., weakest) design for performance testing was feasible. Four parameters were challenged around a nominal TO design point. The tested parameters were penalty factor, volume fraction, element size, and density threshold. TO and AM workflows as well as QOIs are defined to measure the effects. A load frame, 3D-DIC system, and 3D scanner measured the mechanical response and geometric features of the manufactured structure.

Penalty factor and mesh element size were less influential on the construct's reaction force. Volume fraction and density threshold showed a linear relationship with respect to the construct's reaction force, with volume fraction having the largest influence. The von Mises stress and 1st principal strain of the construct's TO region revealed highly non-linear and non-monotonic responses to some of the tested TO workflow parameters. This could make predicting worst-cases within the given parameter limits or extrapolation difficult.

Relatively high errors of 30.0% were observed during local mechanical response validations. These appeared to occur near features that challenged the workflow in terms of technological limitations, such as sharp corners and thin features. While potential explanations for this error are presented, one suggestion may be to ensure that the critical regions (which govern the predicted performance of the part) are in reliable and consistent locations.

An *in silico* TO parameter sensitivity study around a nominal design point may not be sufficient to identify worst-case constructs for performance testing. Additional techniques may need to be applied to ensure that the worst-case performance is benchmarked. One strategy would be to limit the number of TO parameters that are allowed to be modified in the workflows, so that the validation burden is potentially lessened. On the other hand, device generating workflows that involve TO and AM lattices (such as multi-scale topology optimization) may need to consider more workflow parameters to challenge due to the complex features of the desired resultant device.

CRediT authorship contribution statement

Myung Kyun Sung: Writing – review & editing, Writing – original draft, Visualization, Validation, Software, Methodology, Investigation, Formal analysis, Data curation. **Matthew Schwerin:** Writing – review & editing, Writing – original draft. **Yutika Badhe:** Visualization, Validation, Methodology, Investigation, Formal analysis. **Daniel Porter:** Writing – review & editing, Writing – original draft, Visualization, Validation, Supervision, Project administration, Methodology, Investigation, Formal analysis, Conceptualization.

Declaration of competing interest

The authors declare that they have no known competing financial interests or personal relationships that could have appeared to influence the work reported in this paper.

Data availability

Data will be made available on request.

Acknowledgments

The authors would like to thank Andrew Baumann (CDRH), David Hwang (CDRH), and Snehal Shetye (CDRH) for their technical support and guidance throughout this project and the Additive Manufacturing Medical Products (AMMP) core facility for fabricating the samples used in this research. This study was funded by the U.S. FDA Center for Devices and Radiological Health (CDRH) Critical Path program (CDRH Critical Path 2021). This research was also supported in part by an appointment to the Research Participation Program at the U.S. FDA administered by the Oak Ridge Institute for Science and Education (ORISE) through an interagency agreement between the U.S. Department of Energy and FDA.

None of the authors have a conflict of interest to report. The findings and conclusions in this article have not been formally disseminated by the U.S. FDA and should not be construed to represent any agency determination or policy. The mention of commercial products, their sources, or their use in connection with material reported herein is not to be construed as either an actual or implied endorsement of such products by the Department of Health and Human Services.

Appendix A. Supplementary data

Supplementary data to this article can be found online at <https://doi.org/10.1016/j.jmbbm.2023.105844>.

References

- Al-Ali, M.A., Al-Ali, M.A., Takezawa, A., Kitamura, M., 2017. Topology optimization and fatigue analysis of temporomandibular joint prosthesis. *World J. Mech.* 7 (12), 323–339.
- Andreassen, E., Clausen, A., Schevenels, M., Lazarov, B.S., Sigmund, O., 2011. Efficient topology optimization in MATLAB using 88 lines of code. *Struct. Multidiscip. Optim.* 43 (1), 1–16.
- Bendsøe, M.P., 1989. Optimal shape design as a material distribution problem. *Struct. Optim.* 1 (4), 193–202.
- Brackett, D., Ashcroft, I., Hague, R., 2011. Topology optimization for additive manufacturing. *International Solid Freeform Fabrication Symposium. University of Texas at Austin*.
- Cheng, L., Bai, J., To, A.C., 2019. Functionally graded lattice structure topology optimization for the design of additive manufactured components with stress constraints. *Comput. Methods Appl. Mech. Eng.* 344, 334–359. <https://doi.org/10.1016/j.cma.2018.10.010>.
- Deng, Y., Korvink, J.G., 2018. Self-consistent adjoint analysis for topology optimization of electromagnetic waves. *J. Comput. Phys.* 361, 353–376.
- Frazier, W.E., 2014. Metal additive manufacturing: a review. *J. Mater. Eng. Perform.* 23 (6), 1917–1928.
- Gaynor, A.T., Guest, J.K., 2016. Topology optimization considering overhang constraints: eliminating sacrificial support material in additive manufacturing through design. *Struct. Multidiscip. Optim.* 54 (5), 1157–1172. <https://doi.org/10.1007/s00158-016-1551-x>.
- Gaynor, A.T., Meisel, N.A., Williams, C.B., Guest, J.K., 2014. Multiple-material topology optimization of compliant mechanisms created via PolyJet three-dimensional printing. *J. Manuf. Sci. Eng.* 136 (6).
- Gersborg-Hansen, A., Sigmund, O., Haber, R.B., 2005. Topology optimization of channel flow problems. *Struct. Multidiscip. Optim.* 30 (3), 181–192.
- Guest, J.K., Prévost, J.H., 2006. Topology optimization of creeping fluid flows using a Darcy–Stokes finite element. *Int. J. Numer. Methods Eng.* 66 (3), 461–484.
- Guest, J.K., Prévost, J.H., Belytschko, T., 2004. Achieving minimum length scale in topology optimization using nodal design variables and projection functions. *Int. J. Numer. Methods Eng.* 61 (2), 238–254. <https://doi.org/10.1002/nme.1064>.
- Guo, L.-X., Yin, J.-Y., 2019. Finite element analysis and design of an interspinous device using topology optimization. *Med. Biol. Eng. Comput.* 57 (1), 89–98. <https://doi.org/10.1007/s11517-018-1838-8>.
- Im, C.-H., Jung, H.-K., Kim, Y.-J., 2003. Hybrid genetic algorithm for electromagnetic topology optimization. *IEEE Trans. Magn.* 39 (5), 2163–2169.
- Jung, T., Lee, J., Lee, J., 2021. Design and fabrication of magnetic system using multi-material topology optimization. *IEEE Access* 9, 8649–8658. <https://doi.org/10.1109/ACCESS.2021.3049271>.
- Keshavarzzadeh, V., Kirby, R., Narayan, A., 2019. Parametric topology optimization with multiresolution finite element models. *International Journal for Numerical Methods in Engineering* 119 (7), 567–589. <https://doi.org/10.1002/nme.6063>.
- Kuo, Y.-H., Cheng, C.-C., Lin, Y.-S., San, C.-H., 2018. Support structure design in additive manufacturing based on topology optimization. *Struct. Multidiscip. Optim.* 57 (1), 183–195. <https://doi.org/10.1007/s00158-017-1743-z>.
- Langelaa, M., 2016. Topology optimization of 3D self-supporting structures for additive manufacturing. *Addit. Manuf.* 12, 60–70. <https://doi.org/10.1016/j.addma.2016.06.010>.
- Li, S., Yuan, S., Zhu, J., Wang, C., Li, J., Zhang, W., 2020. Additive manufacturing-driven design optimization: building direction and structural topology. *Addit. Manuf.* 36, 101406. <https://doi.org/10.1016/j.addma.2020.101406>.
- Liu, J., Gaynor, A.T., Chen, S., Kang, Z., Suresh, K., Takezawa, A., Li, L., Kato, J., Tang, J., Wang, C.C.L., Cheng, L., Liang, X., To, A.C., 2018. Current and future trends in topology optimization for additive manufacturing. *Struct. Multidiscip. Optim.* 57 (6), 2457–2483. <https://doi.org/10.1007/s00158-018-1994-3>.
- Liu, J., Ma, Y., 2016. A survey of manufacturing oriented topology optimization methods. *Adv. Eng. Software* 100, 161–175. <https://doi.org/10.1016/j.advengsoft.2016.07.017>.
- Liu, K., Tovar, A., 2014. An efficient 3D topology optimization code written in Matlab. *Struct. Multidiscip. Optim.* 50 (6), 1175–1196.
- Martin Philip Bendsøe, N.K., 1988. Generating optimal topologies in structural design using a homogenization method. *Comput. Methods Appl. Mech. Eng.* 71 (2), 197–224. [https://doi.org/10.1016/0045-7825\(88\)90086-2](https://doi.org/10.1016/0045-7825(88)90086-2).
- Montoya-Zapata, D., Acosta, D.A., Moreno, A., Posada, J., Ruiz-Salguero, O., 2019. Sensitivity Analysis in Shape Optimization Using Voxel Density Penalization. *XXIX Spanish Computer Graphics Conference (Ceig19)*, pp. 31–40. <https://doi.org/10.2312/ceig.20191201>.
- Munk, D.J., Auld, D.J., Steven, G.P., Vio, G.A., 2019. On the benefits of applying topology optimization to structural design of aircraft components. *Struct. Multidiscip. Optim.* 60 (3), 1245–1266.
- Neff, C., Hopkinson, N., Crane, N.B., 2015. Selective Laser Sintering of Diamond Lattice Structures: Experimental Results and FEA Model Comparison. *Solid Freeform Fabrication Symposium, Austin, Texas*.
- Ngo, T.D., Kashani, A., Imbalzano, G., Nguyen, K.T.Q., Hui, D., 2018. Additive manufacturing (3D printing): a review of materials, methods, applications and challenges. *Compos. B Eng.* 143, 172–196. <https://doi.org/10.1016/j.compositesb.2018.02.012>.
- PA, 2022. Balance 1.0 Material Datasheet [Datasheet]. <https://eos.materialdatacenter.com/eo/standard/main/ds/0>. Last accessed April 10th, 2023.
- Porter, D.A., Di Prima, M.A., Badhe, Y., Parikh, A.R., 2022. Nylon lattice design parameter effects on additively manufactured structural performance. *J. Mech. Behav. Biomed. Mater.* 125, 104869. <https://doi.org/10.1016/j.jmbbm.2021.104869>.
- Rupp, C.J., Evgrafov, A., Maute, K., Dunn, M.L., 2009. Design of piezoelectric energy harvesting systems: a topology optimization approach based on multilayer plates and shells. *J. Intell. Mater. Syst. Struct.* 20 (16), 1923–1939.
- Sigmund, O., 2001. A 99 line topology optimization code written in Matlab. *Struct. Multidiscip. Optim.* 21 (2), 120–127.
- Sigmund, O., 2007. Morphology-based black and white filters for topology optimization. *Struct. Multidiscip. Optim.* 33 (4–5), 23. <https://doi.org/10.1007/s00158-006-0087-x>.
- Sigmund, O., Petersson, J., 1998. Numerical instabilities in topology optimization: a survey on procedures dealing with checkerboards, mesh-dependencies and local minima. *Struct. Optim.* 16 (1), 68–75.
- Sotola, M., Marsalek, P., Rybansky, D., Fusek, M., Gabriel, D., 2021. Sensitivity analysis of key formulations of topology optimization on an example of cantilever bending beam. *Symmetry* 13 (4). <https://doi.org/10.3390/sym13040712>.
- Stoia, D.I., Marsavina, L., Linul, E., 2019. Correlations between process parameters and outcome properties of laser-sintered polyamide. *Polymers* 11 (11). <https://doi.org/10.3390/polym11111850>.
- Sung, M.K., Lee, S., Burns, D.E., 2022. Robust topology optimization of a flexural structure considering multi-stress performance for force sensing and structural safety. *Struct. Multidiscip. Optim.* 65 (1), 1–21.
- Sutradhar, A., Park, J., Carrau, D., Nguyen, T.H., Miller, M.J., Paulino, G.H., 2016. Designing patient-specific 3D printed craniofacial implants using a novel topology optimization method. *Med. Biol. Eng. Comput.* 54 (7), 1123–1135. <https://doi.org/10.1007/s11517-015-1418-0>.
- Svanberg, K., 1987. The method of moving asymptotes—a new method for structural optimization. *Int. J. Numer. Methods Eng.* 24 (2), 359–373.
- Tyfopoulos, E., Steinert, M., 2020. Topology and parametric optimization-based design processes for lightweight structures. *Appl. Sci.* 10 (13). <https://doi.org/10.3390/app10134496>.
- Vanek, J., Galicia, J.A.G., Benes, B., 2014. Clever support: efficient support structure generation for digital fabrication. *Comput. Graph. Forum* 33 (5), 117–125. <https://doi.org/10.1111/cgf.12437>.
- Wang, M.Y., Wang, X., Guo, D., 2003. A level set method for structural topology optimization. *Comput. Methods Appl. Mech. Eng.* 192 (1–2), 227–246.
- Wong, K.V., Hernandez, A., 2012. A Review of Additive Manufacturing. *International scholarly research notices*, 2012.
- Wu, N., Li, S., Zhang, B., Wang, C., Chen, B., Han, Q., Wang, J., 2021. The advances of topology optimization techniques in orthopedic implants: a review. *Med. Biol. Eng. Comput.* 59 (9), 1673–1689.
- Xiao, Z., Yang, Y., Xiao, R., Bai, Y., Song, C., Wang, D., 2018. Evaluation of topology-optimized lattice structures manufactured via selective laser melting. *Mater. Des.* 143, 27–37. <https://doi.org/10.1016/j.matdes.2018.01.023>.

- Zheng, B., Chang, C.-J., Gea, H.C., 2009. Topology optimization of energy harvesting devices using piezoelectric materials. *Struct. Multidiscip. Optim.* 38 (1), 17–23.
- Zhou, M., Rozvany, G.I.N., 1991. The COC algorithm, Part II: topological, geometrical and generalized shape optimization. *Comput. Methods Appl. Mech. Eng.* 89 (1–3), 309–336.
- Zhu, J.-H., Zhang, W.-H., Xia, L., 2016. Topology optimization in aircraft and aerospace structures design. *Arch. Comput. Methods Eng.* 23 (4), 595–622.
- Zhu, J., Zhou, H., Wang, C., Zhou, L., Yuan, S., Zhang, W., 2021. A review of topology optimization for additive manufacturing: status and challenges. *Chin. J. Aeronaut.* 34 (1), 91–110. <https://doi.org/10.1016/j.cja.2020.09.020>.
- Zillober, C., 1993. A globally convergent version of the method of moving asymptotes. *Struct. Optim.* 6 (3), 166–174.